Photoluminescence properties of $Ca_4La_6(SiO_4)_4(PO_4)_2O_2$-based phosphors for wLEDs

Ju Cheng (程 菊)[1,2], Jia Zhang (张 佳)[1,*], Jian Lu (陆 建)[2,], Xintian Bian (边心田)[1], Hongchao Zhang (张宏超)[2], Zhonghua Shen (沈中华)[2], Xiaowu Ni (倪晓武)[2], Pengcheng Ma (马鹏程)[1], and Jin Shi (施 锦)[1]**

[1]*School of Physics and Electronic Electrical Engineering, Huaiyin Normal University, Huaian 223001, China*
[2]*School of Science, Nanjing University of Science and Technology, Nanjing 210094, China*
**Corresponding author: zhangjianew@126.com; **corresponding author: lj6805@163.com*
Received December 30, 2018; accepted February 22, 2019; posted online May 23, 2019

The apatite compound $Ca_4La_6(SiO_4)_4(PO_4)_2O_2$ (CLSPO) was explored as the host material for phosphors used in white light-emitting diodes (wLEDs). The crystal structure of the CLSPO host prepared by the solid-state reaction method was investigated with Rietveld refinement. The rare earth ions (Eu^{3+}/ Tb^{3+}/Ce^{3+}, Tb^{3+}/Tb^{3+}, Mn^{2+}) activated CLSPO phosphors were synthesized, and their photoluminescence properties, quantum yields, as well as thermal stabilities, were studied. Under near-ultraviolet excitations, the Eu^{3+} and Tb^{3+}-doped CLSPO compounds exhibited red and green emissions with high luminescence efficiencies. Besides, tunable emissions from green to orange were obtained by introducing Mn^{2+} ions into the Tb^{3+}-doped CLSPO samples. The results showed that the phosphors studied may have potential applications for wLEDs.

OCIS codes: 160.4760, 230.3670, 300.6170.
doi: 10.3788/COL201917.051602.

Compared with ordinary lighting equipment, white light-emitting diodes (wLEDs) are regarded as the next generation lighting sources owing to their higher luminous efficiency, longer service life, and lower energy consumption[1,2]. In recent years, there have been some methods for achieving wLEDs[3,4]. One way is to combine a blue InGaN chip with $Y_3Al_5O_{12}$:Ce^{3+} (YAG:Ce) yellow phosphor[3]. However, due to the lack of red luminescence contribution, such wLEDs exhibit some disadvantages, such as low color rendering index (CRI ≈ 70–80) and high correlated color temperature (CCT ≈ 7500 K)[5,6]. Another way often used is to coat trichromatic phosphors on the surface of an ultraviolet (UV) emitting chip[3,4]. By mixing the red, green, and blue light emitted from the phosphors excited by UV light, white light with superior color rendering can be obtained. In this case, the study on high-performance phosphor is important for improving the performance of wLEDs[7].

Rare earth ions play an irreplaceable role in the field of solid-state lighting due to their 5d–4f or 4f–4f transitions[3–5]. The Eu^{3+} and Tb^{3+} ions with strong absorptions in the UV and near-UV regions have been frequently used to achieve red and green components in wLEDs[4–7]. Furthermore, as a transition metal ion, Mn^{2+} generally exhibits a relatively long emission wavelength from the green to red region. As its effective excitation band is in the range of 250 to 500 nm, such an ion can act as an activator in the energy transfer (ET) process[6,8]. Therefore, the researches on the Eu^{3+}, Tb^{3+}, and Mn^{2+}-doped phosphors could show potential application values.

The phosphor host provides the necessary crystal field environment for the electronic transition and spectral emission of rare earth ions, which plays an important role in determining the luminescent properties of rare earth ions[3,9]. The apatite structure compounds (space group $P6_3/m$) with the general formula $M_{10}(EO_4)_6X_2$ ($M = Ca^{2+}$, Sr^{2+}, Ba^{2+}, La^{3+}, Y^{3+}, Gd^{3+}, Mn^{2+}, Na^+, etc.; $E = P^{5+}$, Si^{4+}, As^{5+}, V^{5+}, etc.; and $X = O^{2-}$, OH^-, F^-, Cl^-, etc.) have been extensively used as host materials due to their adjustable crystal structure and high physical and chemical stability[3,8–13]. Eu^{3+} and Tb^{3+} activated apatite structure phosphors have also been widely reported[5–12]. Xia *et al.* have synthesized a series of apatite structure hosts $Ca_{2+x}La_{8-x}(SiO_4)_{6-x}(PO_4)_xO_2$ ($x = 0$, 2, 4, 6) by substituting [La^{3+}–SiO_4^{4-}] for [Ca^{2+}–PO_4^{3-}] in the solid solution $Ca_8La_2(PO_4)_6O_2$ and investigated the effect of the crystal structure evolution on the luminescence properties of Eu^{2+}-doped phosphors[3,13]. Ouenzerfi *et al.* have reported the $Ca_{2+x}La_{8-x}(SiO_4)_{6-x}(PO_4)_xO_2$:$Eu^{3+}$ ($x = 0$, 3, 6) phosphors and studied the site occupation rules[10]. Such hosts contain two kinds of cationic sites, a nine-coordinated 4f site with C_3 point symmetry and a seven-coordinated 6h site with C_s point symmetry, and both sites are suitable for the substitutions of rare earth ions and transition metal ions[5–10]. In this work, the compound $Ca_4La_6(SiO_4)_4(PO_4)_2O_2$ (CLSPO) was chosen as the host, and a series of Eu^{3+}/Tb^{3+} activated phosphors were synthesized via the solid-state reaction method. The crystal structure, bandgap, and luminescence properties were investigated in detail. Ce^{3+}/Mn^{2+} ions were then introduced into CLSPO: Tb^{3+} phosphors. The ET mechanism and the thermal stability of the phosphor were also discussed.

$Ca_4La_{6-x}(SiO_4)_4(PO_4)_2O_2$:$xEu^{3+}$ (CLSPO: xEu^{3+}, $x = 0$–1.20), $Ca_4La_{6-x}(SiO_4)_4(PO_4)_2O_2$:$xTb^{3+}$ (CLSPO: xTb^{3+}, $x = 0$–1.20), $Ca_4La_{5.94-y}(SiO_4)_4(PO_4)_2O_2$:

$0.06Ce^{3+}$, $y Tb^{3+}$ (CLSPO: $0.06Ce^{3+}$, $y Tb^{3+}$, $y = 0$–1.50), and $Ca_{4-y}La_{5.1}(SiO_4)_4(PO_4)_2O_2$: $0.90Tb^{3+}$, $y Mn^{2+}$ (CLSPO: $0.90Tb^{3+}$, $y Mn^{2+}$, $y = 0$–0.68) samples were synthesized with the high-temperature solid-state reaction method. The starting materials, including $CaCO_3$ (99%), $(NH_4)_2HPO_4$ (99%), SiO_2 (99%), La_2O_3 (99.99%), Eu_2O_3 (99.99%), Tb_4O_7 (99.99%), CeO_2 (99.99%), and $MnCO_3$ (99%), were stoichiometrically mixed and grounded thoroughly with an agate mortar. The mixture was first pre-fired in air at 600°C for 3 h, then re-grounded, and calcined at 1400°C for 4 h in a reducing atmosphere (N_2:H_2 = 95:5) for CLSPO: Tb^{3+}, CLSPO: Ce^{3+}, Tb^{3+}, and CLSPO: Tb^{3+}, Mn^{2+}, but in air for CLSPO: Eu^{3+}. The samples were cooled down to room temperature naturally.

The powder X-ray diffraction (XRD) patterns of the products were collected on an ARL X'TRA powder X-ray diffractometer with Cu Kα radiation ($\lambda = 1.5406$ Å, 1 Å = 0.1 nm) operating at 40 kV and 35 mA. Diffuse reflection spectra (DRS) ranging in 200–800 nm were measured with a UV/visible spectrophotometer (UV-3600, SHIMADZU) using $BaSO_4$ as a reference. The photoluminescence excitation (PLE) spectra and photoluminescence (PL) spectra, as well as the temperature dependent measurement, were recorded on an Edinburgh FS5 fluorescence spectrophotometer with a 150 W xenon lamp as the light source. The PL internal quantum yield measurements of the samples were carried out with an integrating sphere in the FS5 spectrophotometer. The fluorescence lifetime was measured on an Edinburgh FLS 920 fluorescence spectrophotometer. The bonding energy of the element was measured by an X-ray photo-electron spectrometer (XPS, ESCALAB 250Xi), and the chemical shifts of XPS peaks were standardized by the C_{1s} peak at 284.6 eV.

Figure 1(a) shows the XRD patterns of the representative samples CLSPO, CLSPO: $0.90Eu^{3+}$, CLSPO: $0.90Tb^{3+}$, CLSPO: $0.90Tb^{3+}$, $0.68Mn^{2+}$, and CLSPO: $0.06Ce^{3+}$, $1.20Tb^{3+}$. All of the diffraction peaks match well with the standard card of $Ca_4La_6(SiO_4)_6(OH)_2$ (JCPDS 20-0217), indicating that the as-synthesized phosphors are single-phased, and the doped Eu^{3+}, Tb^{3+}, Ce^{3+}, or Mn^{2+} ions do not bring significant changes in the crystal structure of the host. For observation, the locally enlarged view of Fig. 1(a) is given in Fig. 1(b). The diffraction peaks of the samples doped with ions present a shift towards high-angle direction compared with the host. This is attributed to the substitution of the La^{3+} ions by smaller $Eu^{3+}/Tb^{3+}/Ce^{3+}$ ions and Ca^{2+} ions by smaller Mn^{2+} ions, and then the cell parameters will be changed after doping. The XRD data of the CLSPO sample was analyzed with the General Structure Analysis System (GSAS) refinement software to obtain the crystal structure, using the structural parameters from the literature as the initial model[3]. Figure 1(c) presents the refinement results, and the main refinement parameters are listed in Table S1 (Table S1, Table S2, and Figs. S1–S5 hereinafter are shown in Supplementary Materials). The cell parameters and

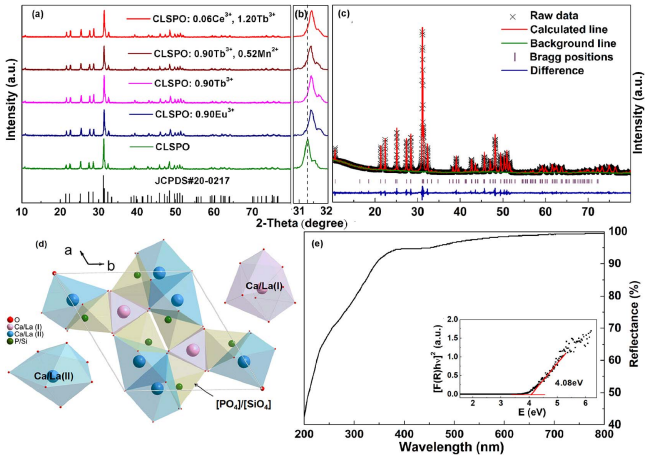

Fig. 1 (a) XRD patterns of the samples. (b) Locally enlarged view of (a). (c) XRD refinement for the CLSPO host. (d) Crystal structure of CLSPO host along the *c*-axis direction, and the coordinated environments of Ca/La(I) and Ca/La(II) atoms. (e) Diffuse reflection spectrum of CLSPO host. Inset: bandgap value of CLSPO obtained with the K–M function and the Tauc relation.

residual factors are $a = b = 9.595$ Å, $c = 7.088$ Å, $V = 565.121$ Å^3, and $\chi^2 = 3.146$, $R_{wp} = 7.58\%$, $R_p = 6.23\%$, implying that the synthesized compound is single-phased and the refined results are consistent with the initial model. Table S2 gives the cell parameters of the representative samples. Due to the difference of ionic radius, the cell volumes of the samples doped with ions are smaller than the CLSPO host. The spatial view of the CLSPO unit cell is presented in Fig. 1(d). In the CLSPO compound, the Ca/La(I) atom located at the 4f site with C_3 symmetry is surrounded by nine O atoms, and each Ca/La(II) atom located at the 6h site in C_s symmetry is connected with seven O atoms[8]. The Si/P atoms are tetrahedrally coordinated by four O atoms, and the SiO_4/PO_4 tetrahedrons connect the 4f tetrakaidecahedrons and 6h hendecahedrons[14]. From the point of view of charge balance and ionic radius similarity, the $Eu^{3+}/Tb^{3+}/Ce^{3+}$ ions are supposed to occupy the La^{3+} sites randomly in the CLSPO matrix, and Mn^{2+} ions are expected to substitute the Ca^{2+} sites[15].

The DRS was measured and shown in Fig. 1(e). The CLSPO host exhibits a high reflectance in the 400–800 nm range, consistent with the white daylight color of the sample. A broad absorption is observed below 350 nm, which is attributed to the charge transfer absorption between the valence band and the conduction band in the host lattice[16].The optical bandgap value E_g can be calculated using the Kubelka–Munk (K–M) function $F(R_\infty)$ and the Tauc relation for direct allowed transitions[17–19]:

$$F(R_\infty) = \frac{(1 - R_\infty)^2}{2R_\infty} = K/S, \tag{1}$$

$$\alpha h\nu \propto (h\nu - E_g)^{1/2}, \tag{2}$$

where R_∞ is the ratio of the light scattered from a thick layer of the sample and an ideal non-absorbing reference sample ($R_{\text{sample}}/R_{\text{reference}}$); $h\nu$ is the photon energy; K, S, and α are the absorption, scattering, and linear absorption coefficients, respectively. For the material, which scatters in a completely diffuse manner (or illuminated at 60° incidence), K can be substituted by 2α, and S can be considered as a constant with respect to the wavelength, so Eq. (2) can be written as $[F(R_\infty)h\nu]^2 \propto (h\nu - E_g)$. The inset of Fig. 1(d) presents the $[F(R_\infty)h\nu]^2$ plot, from which the CLSPO optical bandgap value (4.08 eV) can be traced by extrapolating the linear fit to $[F(R_\infty)h\nu]^2 = 0$.

Figure 2(a) demonstrates the normalized PLE and PL spectra of CLSPO: 0.90Eu^{3+} samples. The PLE spectrum monitored at 613 nm contains a broad band corresponding to the O^{2-}–Eu^{3+} charge transfer band (CTB) and several sharp excitation lines due to the 4f–4f transitions[20]. The peaks located at 361, 381, 393, 411, and 466 nm correspond to the transitions from the ground state $^7F_0$ to $^5D_4$, $^5L_7$, $^5L_6$, $^5D_3$, and $^5D_2$ level, respectively[11,21,22]. The most intense absorption occurs at 393 nm, which implies that the phosphor can be effectively excited in such a wavelength range. Several emission lines peaking at 577, 590, 613, 652, and 701 nm can be observed in the PL spectrum, due to the transitions from $^5D_0$ to ^7F_j ($j = 0$–4) levels of Eu^{3+}, from which the surrounding environments for Eu^{3+} ions can be investigated. The $^5D_0 - {}^7F_0$ and $^5D_0 - {}^7F_2$ transitions are hypersensitive and strongly dependent on the crystal field[23,24]. The forbidden $^5D_0 - {}^7F_0$ transition will appear only when Eu^{3+} occupies a site with local symmetry of C_n, C_{nv}, or C_s, and the number of emission lines corresponding to the transition implies the number of sites Eu^{3+} occupied in the crystal lattice[25]. In the PL spectrum of CLSPO: 0.90Eu^{3+}, one $^5D_0 - {}^7F_0$ transition line can be observed, indicating that Eu^{3+} prefers to substitute Ca/La(II) with C_s symmetry in CLSPO. Furthermore, the emission at 613 nm caused by the $^5D_0 - {}^7F_2$ transition owns the highest intensity, implying that the sites occupied by Eu^{3+} ions are of low symmetry without the inversion center[9].

Figure 2(b) shows the PL spectra of CLSPO: $x$$Eu^{3+}$ ($x =$ 0.06, 0.30, 0.60, 0.90, and 1.20) phosphors. The profile of each spectrum with different Eu^{3+} content is similar, and the PL intensity first increases with x until $x = 0.90$ and then decreases due to the concentration quenching effect. Furthermore, the ratio of red ($^5D_0 - {}^7F_2$) and orange ($^5D_0 - {}^7F_1$) emission intensity (I_R/I_O) is regarded as an index for site asymmetry of the coordination environment around Eu^{3+}. A higher (I_R/I_O) value means a lower symmetry of the crystal field around Eu^{3+} ions and a better color chromaticity[9]. The inset of Fig. 2(b) presents the plots of emission intensity and (I_R/I_O) value versus x, from which it can be noticed that the (I_R/I_O) values of the sample increase from 2.56 to 4.15, indicating the inversion asymmetry of the site that Eu^{3+} occupied is increased, and the color chromaticity is improved.

The internal quantum efficiency (QE) (η_i) of the CLSPO: 0.90Eu^{3+} sample was calculated based on the following equation[26]:

$$\eta_i = \frac{\int \lambda P(\lambda)\,\mathrm{d}\lambda}{\int \lambda [E(\lambda) - R(\lambda)]\,\mathrm{d}\lambda}, \tag{3}$$

where $P(\lambda)$ is the emission spectrum of the sample, and $E(\lambda)$ and $R(\lambda)$ represent the excitation light without and with the sample in the integrating sphere, respectively. Under 393 nm excitation, the internal QE value of the explored CLSPO: 0.90Eu^{3+} phosphor is 64.26%, meaning a bright red emission can be obtained.

The normalized PLE and PL spectra of CLSPO: 0.90Tb^{3+} are shown in Fig. 3(a). The strong excitation band from 250 to 300 nm in the PLE spectrum is derived from the 4f–5d transitions of the Tb^{3+} ions, and other peaks are due to the intra 4f–4f transitions. Monitored at 541 nm, the excitation peaks at 302, 317, 336, 352, 377, and 484 nm are attributed to the $^7F_6 - {}^5H_6$, $^7F_6 - {}^5D_0$, $^7F_6 - {}^5L_7$, $^7F_6 - {}^5D_2$, $^7F_6 - {}^5D_3$, and $^7F_6 - {}^5D_4$ transitions, respectively[5,27], and the strongest one locates at 377 nm. Under 377 nm excitation, the emission peaks in the PL spectrum at 435, 457, 484, 541, 585, and 623 nm are due to the $^5D_3 - {}^7F_4$, $^5D_3 - {}^7F_3$, and $^5D_4 - {}^7F_j$ ($j = 6$–3) transitions of Tb^{3+}, respectively[28]. As the $^5D_4 - {}^7F_5$ transition with green emission is the dominant one, the CLSPO: 0.90Tb^{3+} sample can emit green light under near-UV light excitation. Figure 3(b) shows the PL spectra of CLSPO: $x$$Tb^{3+}$ ($x = 0.06$, 0.30, 0.60, 0.90, and 1.20) samples. As the emissions are ascribed to the 4f–4f transitions of Tb^{3+}, which are

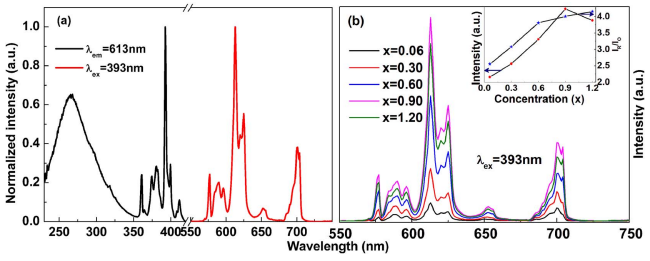

Fig. 2 (a) Normalized PLE and PL spectra of CLSPO: 0.90Eu^{3+} phosphor. (b) PL spectra of CLSPO: $x$$Eu^{3+}$ samples. Inset: the emission intensity and (I_R/I_O) value versus x.

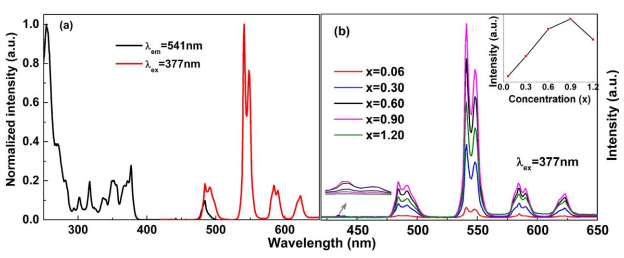

Fig. 3 (a) Normalized PLE and PL spectra of CLSPO: 0.90Tb^{3+} phosphor. (b) PL spectra of CLSPO: $x$$Tb^{3+}$ samples. Inset: the emission intensity versus Tb^{3+} concentration x.

insensitive to the crystal environment, the profiles of the spectra in Fig. 3(b) are similar. As the Tb^{3+} content increases, the emission intensity from the $^5D_3$ level transition decreases, see the magnified view, which shows a different mode of variation from the $^5D_4$ level, mainly due to the cross relaxation process: $^5D_3 + {}^7F_6 \rightarrow {}^5D_4 + {}^7F_0$[29]. The emission intensity of the $^5D_4 - {}^7F_j$ transition in CLSPO: xTb^{3+} phosphors first increases with x and then decreases due to the concentration quenching effect. It can be noticed from the inset of Fig. 3(b) that the most intense emission can be obtained when $x = 0.90$. According to Eq. (3), the internal QE value of the CLSPO: 0.90Tb^{3+} phosphor excited at 377 nm was measured and calculated to be 58.23%, meaning that it can be efficiently pumped with near-UV light.

The inset of Fig. 3(a) shows the PL spectrum of CLSPO: 0.06Ce^{3+} sample, which exhibits a broad band from 350 to 500 nm. It overlaps with the PLE spectrum of the Tb^{3+}-doped CLSPO sample, indicating the possibility of ET from Ce^{3+} to Tb^{3+} when they are co-doped in the host. To investigate this, a series of CLSPO: 0.06Ce^{3+}, yTb^{3+} ($0 \le y \le 1.50$) samples were synthesized and the PL spectra are presented in Fig. S1. The spectra consist of two parts: the emission band of Ce^{3+} and the emission lines from Tb^{3+}. As y increases, the intensity of Tb^{3+} emission increases at first, reaching the maximum when $y = 1.20$, and then decreases due to the concentration quenching effect, shown in the inset of Fig. S1. For Ce^{3+}, the emission intensity deceases gradually, which gives the evidence of ET between the two ions in the CLSPO host. Systematic investigation for the ET process will be carried out in future work.

It is well known that the ET generally exists in Tb^{3+}, Mn^{2+} co-doped phosphors, and tunable emitting light colors could be achieved[29,30]. As the PL properties of Mn-ion-doped phosphor depend deeply on its valence state, it is necessary to verify the existing state of Mn in the matrix for the Tb^{3+}, Mn^{2+}-doped CLSPO system. Fig. S2 shows the XPS spectrum of the CLSPO: 0.90Tb^{3+}, 0.52Mn^{2+} phosphor in the $2p_{3/2}$ and $2p_{1/2}$ regions of Mn. The binding energy of 641.1 and 653.2 eV indicates that the Mn ion has a +2 oxidation state, which is in agreement with that of MnO[31]. For assessing the possible ET between Tb^{3+} and Mn^{2+} ions in the CLSPO host, Fig. 4(a) presents the PLE spectrum of CLSPO: 0.40Mn^{2+} monitored at 604 nm and its PL spectrum excited at 407 nm. For comparison, the CLSPO: 0.90Tb^{3+} upon 377 nm excitation is also presented. The main excitation peaks at 302, 342, 375, 407, 443, and 486 nm are due to the transitions from the $^6A_1(^6S)$ level to the $^4T_1(^4P)$, $^4E(^4D)$, $^4T_2(^4D)$, $[^4A_1(^4G), {}^4E(^4G)]$, $^4T_2(^4G)$, and $^4T_1(^4G)$ energy levels of Mn^{2+}, respectively[1,32]. Under 407 nm excitation, the Mn^{2+}-doped CLSPO phosphor exhibits a broadband emission due to the $^4T_1(^4G) \rightarrow {}^6A_1(^6S)$ transition around 600 nm. It can be noticed that there is an overlap between the PLE spectrum of CLSPO: 0.40Mn^{2+} and the PL spectrum of CLSPO: 0.90Tb^{3+}, indicating the possible ET between

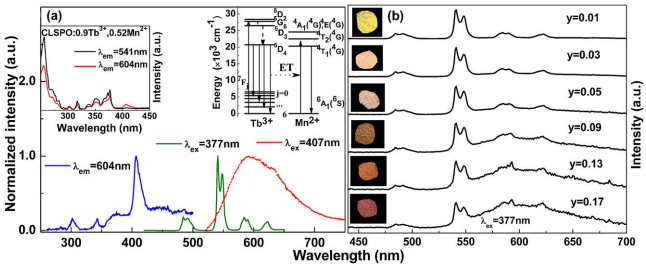

Fig. 4 (a) Normalized PLE (blue line) and PL (red line) spectra of CLSPO: 0.40Mn^{2+}, PL spectrum (green line) of CLSPO: 0.90Tb^{3+}. Insets: left, PLE spectra of CLSPO: 0.90Tb^{3+}, 0.52Mn^{2+} monitored at different wavelengths; right, the schematic of ET from Tb^{3+} to Mn^{2+} in the CLSPO host. (b) PL spectra of CLSPO: 0.90Tb^{3+}, xMn^{2+} samples and the photos of the samples under 365 nm lamp.

the Tb^{3+} and Mn^{2+} ions if they were co-doped in the CLSPO host. A series of CLSPO: 0.90Tb^{3+}, yMn^{2+} ($0 \le y \le 0.68$) samples were then prepared. The PLE spectra of CLSPO: 0.90Tb^{3+}, 0.52Mn^{2+} monitored at 541 and 604 nm are presented in the upper-left inset of Fig. 4(a). The two spectra have almost the same profile as the PLE spectrum of CLSPO: 0.90Tb^{3+} monitored at 541 nm, except the weak band around 407 nm, implying the existence of ET from Tb^{3+} to Mn^{2+}. The ET process can be explained with the energy level schematics of Tb^{3+} and Mn^{2+} in the upper-right inset of Fig. 4(a). Under 377 nm excitation, the Tb^{3+} ions can be excited to the $^5G_6$ level and then relax non-radiatively to the $^5D_3$ and further to the $^5D_4$ level[29]. The transition energy between the $^5D_4$ and $^7F_6$ levels of Tb^{3+} is similar to that from the $^6A_1(^6S)$ to $^4T_1(^4G)$ level of Mn^{2+}, which indicates that more electrons can be excited to the $^4T_1(^4G)$ level, and then the emission intensity can be enhanced. Figure 4(b) presents the PL spectra of CLSPO: 0.90Tb^{3+}, yMn^{2+} ($0 < y \le 0.68$) under 377 nm excitation. Sharp emission peaks due to the $^5D_4 \rightarrow {}^7F_j$ transitions of Tb^{3+} ions can be clearly observed; besides, with the increase of Mn^{2+} concentration, the luminescence intensity of Tb^{3+} gradually decreased, and an orange emission band owing to Mn^{2+} ions appeared. For the CLSPO: 0.90Tb^{3+}, 0.52Mn^{2+} sample, the emission at 604 nm is mainly attributed to Mn^{2+} ions; however, its PLE spectrum shows the typical excitation peaks of Tb^{3+} ions, indicating the possible existence of ET from Tb^{3+} to Mn^{2+}.

The efficiency of ET (η_{ET}) from a sensitizer to an activator can be calculated with the following equation[33,34]:

$$\eta_{ET} = 1 - \tau_s/\tau_{s0}, \tag{4}$$

where τ_{s0} and τ_s represent the decay lifetimes of the sensitizer (Tb^{3+}) in the absence and presence of the activator (Mn^{2+}). Figure S3 shows the decay curves of Tb^{3+} emission at 541 nm in CLSPO: 0.90Tb^{3+}, yMn^{2+} samples excited at 377 nm. The average lifetimes were calculated and presented in Fig. S3(a) using $\tau = \int_0^\infty I(t)t\,dt / \int_0^\infty I(t)\,dt$, where $I(t)$ is the fluorescence intensity at time t. With

the increase of Mn^{2+} concentration, the decay lifetime of Tb^{3+} decreases, indicating the existence of ET from Tb^{3+} to Mn^{2+} in the phosphors. Upon increasing Mn^{2+} concentration, the distance between Tb^{3+} and Mn^{2+} decreases, and then the ET will be more efficient. Using Eq. (4), the ET efficiencies were calculated and given in Fig. S3(b). η_{ET} increases with y, and it can reach 54.6% when $y = 0.68$, implying that an efficient ET has occurred, which will act on the tunable emission in the CLSPO: $0.90Tb^{3+}$, yMn^{2+} phosphors. The photos in Fig. 4(b) illustrate the tunable emissions from yellowish green to orange.

The interaction mechanism of ET from Tb^{3+} to Mn^{2+} in the CLSPO host can be investigated based on Dexter's ET formula and Reisfeld's approximation[35]:

$$\eta_0/\eta \propto C^{n/3}, \tag{5}$$

where η_0 and η are the luminescence QE of Tb^{3+} in the absence and presence of Mn^{2+}, C is the total content of Tb^{3+} and Mn^{2+} ions. From the value of n, the interaction mechanism of the ET process can be deduced. $n = 3$ corresponds to the exchange interaction, and $n = 6$, 8, and 10 indicate the dipole-dipole, dipole-quadrupole, and quadrupole-quadrupole interactions, respectively[1]. The ratio of emission intensities I_0/I can generally be used to assess the value of η_0/η, and then the plots of I_0/I versus $C^{n/3}$ are shown in Figs. S4(a)–S4(c). The optimal linear relation can be obtained when $n = 10$ ($R^2 = 0.9964$), indicating that the ET from Tb^{3+} to Mn^{2+} occurs through the quadrupole-quadrupole interaction.

The emission spectra of the CLSPO: $0.90Eu^{3+}$, CLSPO: $0.90Tb^{3+}$, and CLSPO: $0.90Tb^{3+}$, $0.52Mn^{2+}$ samples were measured at different temperatures and shown in Figs. S5(a)–S5(c). As the temperature increased, the intensity of each sample showed a gradual decrease due to thermal quenching caused by electron–phonon interaction[6,36]. For Eu^{3+} and Tb^{3+} single-doped CLSPO phosphors, the spectral profiles change little upon heating. However, for the Tb^{3+} and Mn^{2+} co-doped phosphor, the Tb^{3+} emission intensity showed good stability, but the Mn^{2+} emission intensity decreased continuously with increasing temperature. This is mainly due to the decrease of ET from Tb^{3+} to Mn^{2+}[30]. When the temperature is raised, the lattice vibration increases, which will enhance the non-radiative transition of the activator, and then the ET efficiency from Tb^{3+} to Mn^{2+} will decrease, resulting in a gradual decrease in the Mn^{2+} emission intensity. The corresponding temperature dependences of the integrated emission intensities of Eu^{3+} and Tb^{3+}-doped phosphors are depicted in the insets of Figs. S5(a) and S5(b). The CLSPO: $0.90Tb^{3+}$ phosphor exhibits a good thermal stability, and the integrated emission intensity at 150°C retains 88.33% of the initial value measured at 25°C. However, only about 56.23% of the initial emission intensity of CLSPO: Eu^{3+} remains when heated to 150°C; hence, further studies will be necessary to improve the thermal stability. For the CLSPO: $0.90Tb^{3+}$, $0.52Mn^{2+}$ phosphor, the emission intensity of Tb^{3+} and Mn^{2+} ions at 150°C decreased to 85.03% and 32.38% of the value at 25°C, respectively, and the integrated emission intensity of CLSPO: $0.90Tb^{3+}$, $0.52Mn^{2+}$ decreased to 56.12%, as shown in Fig. S5(d).

The activation energy (ΔE) of thermal quenching behavior can be calculated using the Arrhenius equation[5]:

$$I(T) = \frac{I_0}{1 + A\exp\left(-\frac{\Delta E}{kT}\right)}, \tag{6}$$

where I_0 is the original emission intensity of the phosphor at room temperature, $I(T)$ is the intensity at a given temperature, A is a constant for a particular host, and k refers to the Boltzmann constant (8.629×10^{-5} eV). From the slope of the curve of $\ln[(I_0/I_T) - 1]$ versus $1/(kT)$, ΔE can be acquired. As shown in the insets of Figs. S5(a) and S5(b), according to the slope of the linear fitting line, the ΔE values of the Eu^{3+} and Tb^{3+}-doped CLSPO phosphors were obtained to be 0.30 and 0.24 eV, respectively.

The Commission International de l'Eclairage (CIE) 1931 chromaticity coordinates of the synthesized samples were calculated according to the emission spectra, as shown in Fig. 5. Excited by near-UV light, the Eu^{3+} and Tb^{3+} activated CLSPO phosphors can present red and green emission colors. The CIE coordinates of the CLSPO: $0.90Tb^{3+}$, yMn^{2+} series under 377 nm excitation vary from the green region (0.3353, 0.5831) to the orange region (0.5173, 0.4446) when y increases from 0 to 0.68. A tunable emission can be obtained by changing the Mn^{2+} content.

A series of CLSPO: $xEu^{3+}/xTb^{3+}/0.90Tb^{3+}$, yMn^{2+} phosphors have been synthesized with the solid-state method. The crystal structure of the CLSPO host was investigated with Rietveld refinement, and the bandgap was explored using the DRS. The PL properties, quantum yields, thermal stabilities, and the CIE coordinates of the synthesized phosphors were then studied. Under near-UV light excitation, the Eu^{3+} and Tb^{3+}-doped CLSPO phosphor can present red and green emissions. Furthermore, due to ET, the emission color can be varied

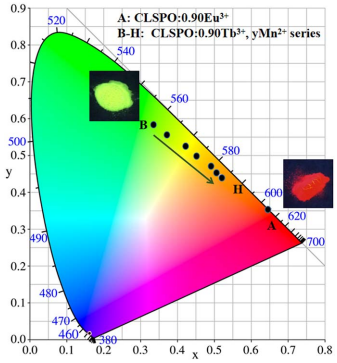

Fig. 5 CIE chromaticity diagram for CLSPO: $0.90Eu^{3+}$ (Point A) and CLSPO: $0.90Tb^{3+}$, yMn^{2+} (Points B–H). Photos: Eu^{3+}/Tb^{3+}-doped CLSPO phosphors under 365 nm UV lamps.

from green to orange by tuning the Mn^{2+} content in the Tb^{3+} and Mn^{2+} co-doped CLSPO phosphor. We believe that based on the current results, some references can be provided to develop new apatite phosphors for wLED applications.

This work was supported by the National Natural Science Foundation of China (Nos. 11604115 and 11547023), the Educational Commission of Jiangsu Province of China (Nos. 18KJB140002 and 17KJA460004), and the Huaian Science and Technology Funds (No. HAC201701).

References

1. X. Zhang, Z. Guo, and M. Gong, Ceram. Int. **43**, 1383 (2017).
2. R. J. Li, X.D. Xu, L.B. Su, Q.L. Sai, C. T. Xia, Q. H. Yang, J. Xu, A. Strzep, and A. Pókoszek, Chin. Opt. Lett. **14**, 021602 (2016).
3. Y. Xia, J. Chen, Y. Liu, M. Molokeev, G. Ming, Z. Huang, and M. Fang, Dalton T. **45**, 1007 (2016).
4. C. Ji, Z. Huang, X. Tian, W. Xie, J. Wen, H. He, C. Zhou, and T. Zeng, Dyes Pigments **160**, 772 (2019).
5. J. Cheng, J. Zhang, H. Zhang, S. Maryam, X. Bian, Z. Shen, X. Ni, and J. Lu, Chin. Opt. Lett. **15**, 121602 (2017).
6. M. Jiao, Q. Xu, Y. Xu, Y. Li, C. Yang, and M. Liu, Ceram. Int. **44**, 15243 (2018).
7. D. A. Hakeem, J. W. Pi, G. W. Jung, S. W. Kim, and K. Park, Dyes Pigments **160**, 234 (2019).
8. Y. Tian, Y. Wei, Y. Zhao, Z. Quan, G. Li, and J. Lin, J. Mater. Chem. C **4**, 1281 (2016).
9. J. Zhong, D. Chen, H. Xu, W. Zhao, J. Sun, and Z. Ji, J. Alloy. Compd. **695**, 311 (2017).
10. R. El Ouenzerfi, G. Panczer, C. Goutaudier, M. T. Cohen-Adad, G. Boulon, M. Trabelsi-Ayedi, and N. Kbir-Ariguib, Opt. Mater. **16**, 301 (2001).
11. Y. Shen, R. Chen, F. Xiao, H. Sun, A. Tok, and Z. Dong, J. Solid State Chem. **183**, 3093 (2010).
12. Q. Guo, L. Liao, L. Mei, H. Liu, and Y. Hai, J. Solid State Chem. **225**, 149 (2015).
13. Y. Xia, Y. Liu, Z. Huang, M. Fang, M. S. Molokeev, and L. Mei, J. Mater. Chem. C **4**, 4675 (2016).
14. H. Liu, Y. Luo, Z. Mao, L. Liao, and Z. Xia, J. Mater. Chem. C **2**, 1619 (2014).
15. R. D. Shannon, Acta Crystallogr. A. **32**, 751 (1976).
16. Y. Fang, F. Liu, J. Hou, Y. Zhang, X. Zheng, N. Zhang, G. Zhao, M. Liao, G. Dai, M. Long, and Y. Liu, J. Lumin. **177**, 280 (2016).
17. J. Zhang, B. Ji, and Z. Hua, Opt. Mater. Express **6**, 3470 (2016).
18. J. Tauc and A. Menth, J. Non-Cryst. Solids **8**, 569 (1972).
19. A. Balakrishna, V. Kumar, A. Kumar, and O. M. Ntwaeaborwa, J. Alloy. Compd. **686**, 533 (2016).
20. X. Min, Z. Huang, M. Fang, Y. Liu, C. Tang, and X. Wu, Inorg. Chem. **53**, 6060 (2014).
21. Z. Wang, P. Li, Z. Yang, and Q. Guo, Mater. Lett. **126**, 89 (2014).
22. A. Dobrowolska, E. C. Karsu, A. J. J. Bos, and P. Dorenbos, J. Lumin. **160**, 321 (2015).
23. G. Blasse, A. Bril, and W. C. Nieuwpoort, J. Phys. Chem. Solids. **27**, 1587 (1966).
24. N. Lakshminarasimhan and U. V. Varadaraju, J. Phys. Chem. Solids **177**, 3536 (2004).
25. G. Blasse and A. Bril, Philips Res. Repts. **21**, 368 (1966).
26. W. Li, R. Xie, T. Zhou, L. Liu, and Y. Zhu, Dalton T. **43**, 6132 (2014).
27. P. Miluski, M. Kochanowicz, J. Zmojda, and D. Dorosz, Chin. Opt. Lett. **15**, 070602 (2017).
28. H. L. Li, Z. L. Wang, S. J. Xu, and J. H. Hao, J. Electrochem. Soc. **156**, J112 (2009).
29. J. Zhang, B. Zhou, and X. Wang, Spectrochim. Acta A **165**, 85 (2016).
30. J. Zhang, Z. Hua, and H. Jiao, Mater. Res. Bull. **95**, 570 (2017).
31. M. C. Biesinger, B. P. Payne, A. P. Grosvenor, L. W. M. Lau, A. R. Gerson, and R. S. C. Smart, Appl. Surf. Sci. **257**, 2717 (2011).
32. L. Jiang, R. Pang, D. Li, W. Sun, Y. Jia, H. Li, J. Fu, C. Li, and S. Zhang, Dalton T. **44**, 17241 (2015).
33. X. Zhang, J. Xu, and M. Gong, J. Lumin. **183**, 348 (2017).
34. J. Cheng, J. Zhang, J. Lu, H. C. Zhang, S. Maryam, Z. H. Shen, X. W. Ni, X. T. Bian, P. C. Ma, and J. Shi, Opt. Mater. Express **8**, 1850 (2018).
35. D. L. Dexter and J. H. Schulman, J. Chem. Phys. **22**, 1063 (1954).
36. K. Li, M. Shang, Y. Zhang, J. Fan, H. Lian, and J. Lin, J. Mater. Chem. C **3**, 7096 (2015).